5.6 Crystallography/High Pressure Science

5-6-1 Crystallography

Crystallography includes various fields in physics, chemistry, mineralogy and biology relating with atomic structure and/or electron distribution of crystalline materials determined by diffraction technique. Therefore the topics based on crystallography come across in the sections of Materials Science, Surfaces and Interfaces, High Pressure Science as well as Biological Science.

This report collects four topics corresponding to Weissenberg method at BL-1A, four circle diffractometry at BL-10A, powder diffractometer at BL-4B2 and Laue method with polychromatic synchrotron radiation at BL-4B1.

Open-mouthed C_{60} Swallows a Hydrogen Molecule

In order to carry out research into the use of molecular capsules as hydrogen storage materials or for medicinal applications, techniques to insert gas or unstable molecules into a molecular cage must be developed. Fullerene, C_{60} is a typical soccer-ball-shape cage molecule, and the organic synthesis of endohedral C_{60} at will is a challenging task. Prof. Komatsu's group recently succeeded in the 100% incorporation of H_2 molecules into derivatives of aza-thia open-cage fullerenes (ATOCF), as shown in Fig. 1[1]. This compound can be regarded as a nano-sized container for a single hydrogen molecule, with which we can store hydrogen at controlled pressure and temperature. The extraordinary high-field shift of the 1H NMR signal of the H_2 molecule reported in [1] surely indicates that H_2 is encapsulated somewhere inside the fullerene cage. However, more substantial information is needed concerning the location of the H_2 molecule within the cage of ATOCF, and this information can be obtained only through the direct observation of the molecule. X-ray diffraction analysis using synchrotron radiation appeared most suitable for this purpose, and we have obtained accurate X-ray diffraction data using a Weissenberg type imaging-plate detector at BL-1A. From X-ray diffraction analysis of a single crystal, we have succeeded in the direct

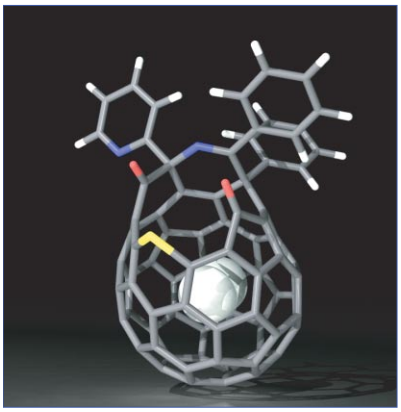

Figure 1
Molecular structure of H_2 @ATOCF. The encapsulated H_2 molecule is shown as a space-filled model.

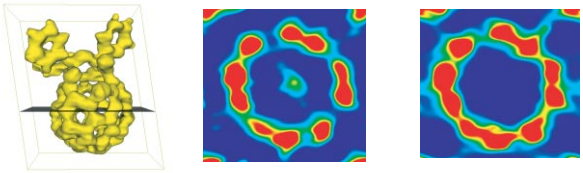

Figure 2
Maximum Entropy Method electron densities of H_2@ATOCF (center) and empty ATOCF (right) , shown as equal-density contour surfaces. The contour maps are drawn over the range 0.01e/Å^3 to 0.11e/Å^3 as indicated in the left-hand panel.

observation of a single floating H_2 molecule inside of the hollow cavity of this fully H_2-encapsulating ATOCF molecule(Fig. 2)[2]. The number of electrons belonging to encapsulated H_2, estimated by integration from the center of the cage to the point of minimum electron density, turned out to be 2.0±0.1. This result exactly corresponds to the presence of one H_2 molecule at the center of the hollow cage of the ATOCF molecule, in excellent agreement with the ^{1}H NMR result[1], demonstrating that this H_2-encapsulating compound is the first material which can allow us to determine the physical properties of single floating H_2 molecule.

Charge Ordering of Eu_3S_4 Deter mined from the X-ray Valence Contrast between Eu^{2+} and Eu^{3+}

Eu_3S_4 is a mixed-valence compound and recognized as a unique system containing divalent rare-earth ions. It has a Th_3P_4-type structure with the space group of *I*43*d* at room temperature, where divalent Eu^{2+} ($4f^7 5s^2 5p^6 \underline{6s^2}$) and trivalent Eu^{3+} ($4f^6 5s^2 5p^6 \underline{5d^1 6s^2}$) ions occupy a crystallographic site in a bcc lattice (Fig. 3a) [3]. The transport properties are characteristic of an intrinsic semiconductor, with the hopping of 4*f* electrons between adjacent Eu sites. The origin of the hopping motion of the charge carriers is considered as either thermally activated drift mobility or electron tunneling.

Eu_3S_4 has a non-magnetic phase transition at a temperature of T_c = 188.5 K as shown in Fig. 4 [4,5]. In Mössbauer spectra of $^{151}Eu_3S_4$ below T = 210 K, two absorption peaks were observed and interpreted as being due to electron hopping between Eu^{2+} and Eu^{3+} ions [6]. An X-ray powder diffraction study [9] found a 0.4% distortion in the ratio of *a/c* for the low-temperature phase. A charge-ordered tetragonal cell was topologically derived from the Th_3P_4 structure (Carter model) [7]. On the other hand, the failure to observe extra phonon modes in Raman scattering is inconsistent with the charge order-disorder transition model [8].

To understand the origin of the phase transition of Eu_3S_4, we have determined the crystal structure and cation distribution of Eu^{2+} and Eu^{3+} in the low-temperature phase by a single-crystal X-ray diffraction study [9]. The growth of twinned crystals was avoided by cooling with a magnetic field.

Fig. 3(b) shows a (001)-projection of the crystal structure of the low-temperature phase of Eu_3S_4 determined at T = 160 K. The crystal symmetry is tetragonal with

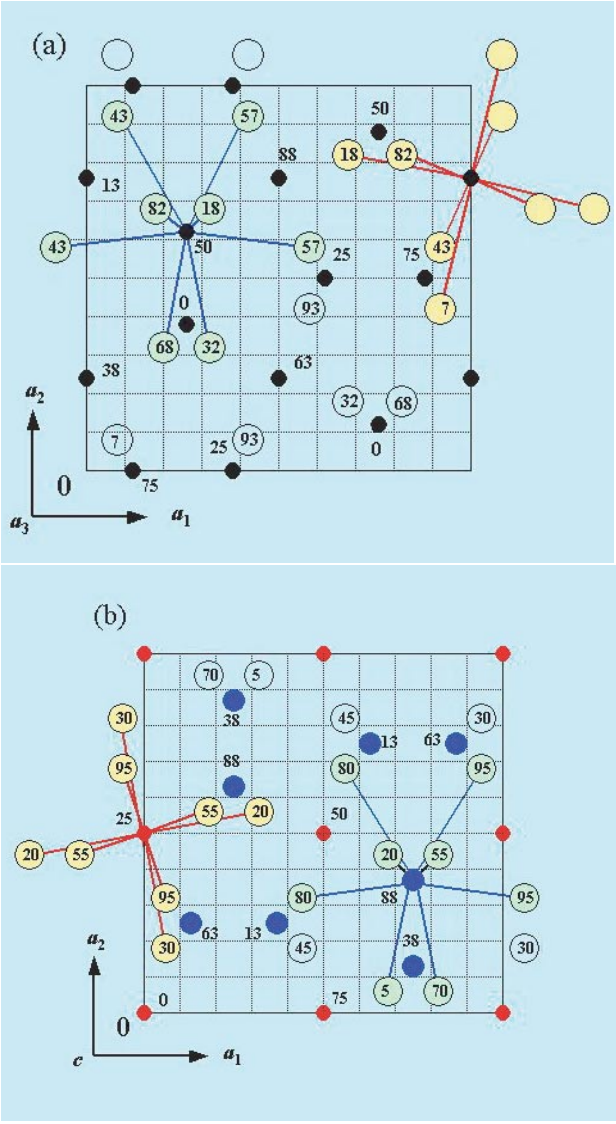

Figure 3
Crystal-structure projection of (a) room-temperature (T = 300 K) and (b) low-temperature (T = 160 K) phases of Eu_3S_4. (a) Black solid circle = Eu (12*a* sites), open circle = S (16*c*), (b) red solid circle = Eu (4*a*), blue solid circle = Eu (8*d*), open circle = S (16*e*). The heights of the atoms on the projection axis are given by integers, which should be multiplied by 100.

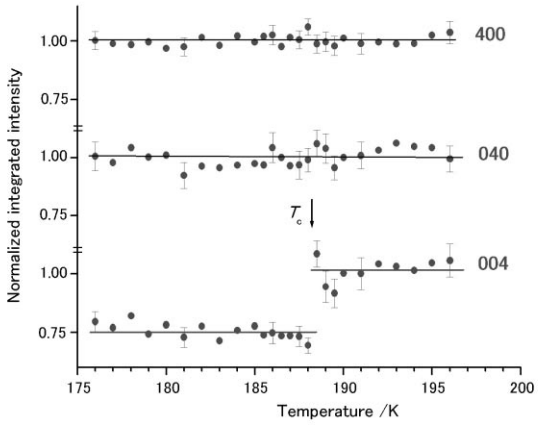

Figure 4
Temperature dependence of the 400, 040 and 004 Bragg intensities of Eu_3S_4. A discontinuity at T_c= 188.5 K can be observed only for the 004 reflection.

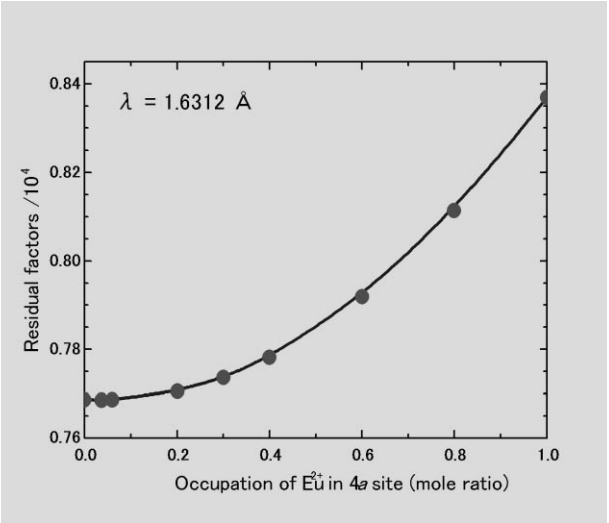

Figure 5
Residual factors in the refinements with the Synchrotron X-ray data measured at λ= 1.6312 Å and T = 180 K, given as a function of the mole ratio of Eu^{2+} ions occupied in the 4*a* sites in the $I\bar{4}2d$ structure.

a space group of $I\bar{4}2d$ and the cell dimensions are a = 8.508 ± 0.001 Å and c = 8.514 ± 0.002 Å. The crystal structure has two different kinds of Eu sites, defined as 4*a* and 8*d* sites, which can both be well represented by the Carter model [7]. Both Eu sites coordinate eight sulfur atoms, where the EuS_8 polyhedra are similar to the distorted cube of the room-temperature phase. Making a comparison between Fig. 3(a) and 3(b), it is clearly seen that the Eu ions maintain similar surroundings with sulfur through the phase transition.

X-ray intensity measurements for valence-difference contrast (VDC) analyses were made using a spherical single crystal at BL-10A. Wavelength slightly longer than the L_{II} absorption edge of Eu were selected for the VDC method, in order to keep a large difference in *f'* between Eu^{2+} and Eu^{3+} but the absorption effect small. Measurements of X-ray absorption near edge structure (XANES) spectra were performed at BL-3A to estimate the experimental-base f' values from f'' and the Kramers-Krönig's dispersion relation.

The cation distribution of Eu^{2+} and Eu^{3+} was determined by crystal-structure analyses based on the intensity data collected at wavelengths of λ = 1.6312 and 1.6298 Å. Least-squares structural refinements suggest that the most plausible atomic arrangement is $[Eu^{3+}]^{4a}[Eu^{2+}Eu^{3+}]^{8d}S_4$. The variation of residual factors is plotted in Fig. 5 as a function of Eu^{2+} content in 4*a* sites. The curve of the residual factors has a minimum, which is close to zero for the occupancy of Eu^{2+} ions at 4*a* sites. This implies that Eu^{2+} ions do not occupy the 4*a* sites. Namely, the charge-ordering scheme is that a half of the Eu^{3+} ions occupy the whole 4*a* sites, while the remaining half of the Eu^{3+} ions mix with Eu^{2+} in 8*d* sites.

Design, Fabrication and Performance of a New Furnace for High-resolution Synchrotron Radiation Powder Diffraction Studies up to 1900 K – An Application to Determine the Electron-density Distribution of Cubic $CaTiO_3$ Perovskite at 1674 K

It is an important challenge to carry out accurate structural analysis using *in situ* diffraction data obtained from materials at high temperatures. Laboratory-based X-ray powder diffractometry using Bragg-Brentano geometry encounters some serious difficulties for high-temperature structural analysis. Synchrotron radiation powder diffraction can overcome these difficulties. Some research groups have previously performed *in situ* synchrotron radiation powder diffraction experiments above 1000 K, however there has been very little work on precise analysis leading to electron-density distributions above 1000 K.

A new electric furnace to measure high-resolution synchrotron radiation powder diffraction profiles from materials at high temperatures up to 1900 K in air has been designed and fabricated (Figs.6 and 7) [10, 11]. The furnace consists of a ceramic refractory with $MoSi_2$ heaters, a water-cooled aluminium body and an automatic sample stage (Fig. 6). We have carried out synchrotron radiation powder diffraction experiments with X-rays of wavelength 0.99945 Å at BL-3A. Diffraction data for a $CaTiO_3$ powder sample at 1674 K in air were collected in the asymmetric flat-type reflection geometry. This method has the following merits: (i) correction for the absorption effect is not necessary in the structural refinement, (ii) the sample temperature does not change during the 2θ scanning, in contrast to the symmetric $2\theta/\theta$ scanning technique (the temperature was maintained with stability ±0.1 K using a thermocouple temperature control), and (iii) there is little reaction between the specimen and its holder at high temperatures.

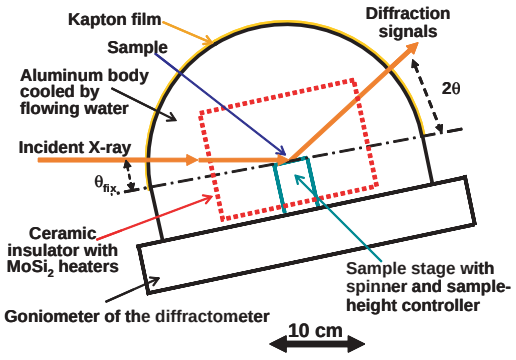

Figure 6
Schematic diagram of the furnace designed and fabricated in the present work [10].

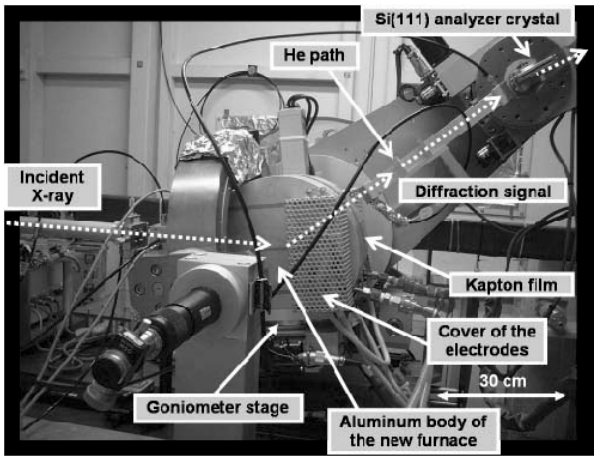

Figure 7
Photo of the new furnace installed at BL-3A [10]. White dashed lined with arrows denote the incident X-ray beam and diffracted signals.

In the synchrotron-radiation-diffraction data of $CaTiO_3$ obtained at 1674 K, the background intensity was extremely low (7-24 counts) compared to the strongest peak intensity (30127 counts). Thus, the present furnace is useful to investigate accurately the intensity data of very weak peaks near a phase transition or due to significant temperature factors at high temperatures. The full-widths at half-maximum of the diffraction peaks at 1674 K ranged from 0.0087 to 0.0197 deg, indicating a high angular resolution. The corresponding $\delta d/d$ values range from 0.041 to 0.118 %, where d and δd are the lattice spacing and peak width in the d scale. Rietveld refinement for the diffraction data of the $CaTiO_3$, perovskite was successfully refined by the ideal cubic $Pm\bar{3}m$ perovskite-type structure (Fig. 8A). The goodness of fit was 1.05, indicating extremely good fitting. The refined unit-cell parameter was 3.89846(1) Å at 1674 K. We could also refine the anisotropic thermal parameters: β_{11}= 0.117(3), β_{22} =β_{33}=0.106(2) and β_{12}

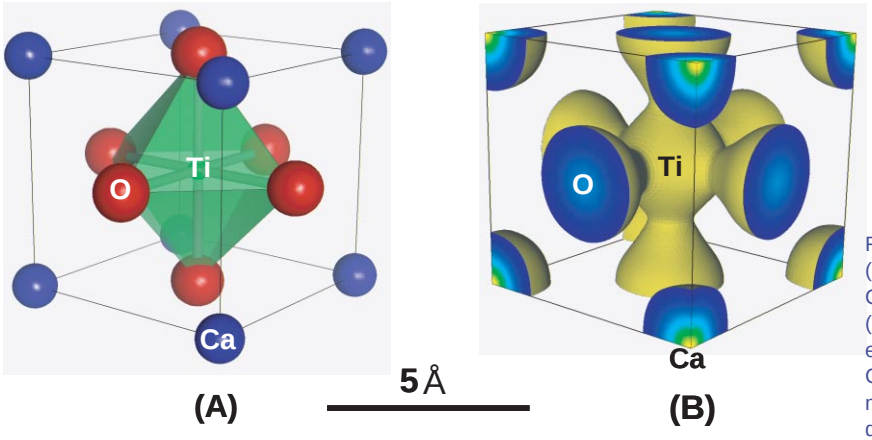

Figure 8
(A) Refined crystal structure of cubic CaTiO3 perovskite at 1674 K in air [10]. (B) Electron-density distribution with equicontour surface at 1.0 e/Å^3 of the cubic $CaTiO_3$ at 1674 K [10]. These fitures were made using the computer program *VENUS* developed by Dianian and Izumi [12].

$=\beta_{23}$ $=\beta_{31}=0$. The electron-density distribution of this sample was successfully obtained by the maximum-entropy method (MEM) and MEM-based pattern fitting. The *R*-factor R_B was improved from 8.27 (Rietveld refinement) to 7.45% (whole pattern fitting with the MEM structure factors). Also R_F was improved from 6.57 to 5.38%. The electron density between the Ti and O atoms shows features characteristic of covalent bonding (Fig. 8B), which might be formed by the hybridization of the Ti-3*d* and O-2*p* electrons. There was much less electron density between the Ca and O atoms, indicating that the Ca atoms are isolated and more ionic. These results clearly show that the present high-temperature synchrotron radiation powder diffraction system yields high-quality data for Rietveld and MEM analyses.

New Modifications of Pyrrhotite Series Found in Interplanetary Dust Particle

Iron-nickel sulfides are the only phases present in all types of extraterrestrial materials. If sulfides in chondritic meteorites and interplanetary dust particles (IDPs) could be properly characterized in compositions, structures and parageneses, there would be a tremendous gain in our understanding of the early solar system history.

Analysis of chondritic interplanetary dust particle L2005 AE6

The chemical formula of this sample was determined to be $Fe_{0.89}Ni_{0.02}S$, analyzed with an electron prove micro analyzer (EPMA).

The diffraction experiment was carried out in a vacuum of 6×10^{-2} Torr by using diffraction equipment developed at BL-4B1 for a micrometer-sized specimen and a micro-area of a larger sample. The Laue pattern was obtained by a 30-min. exposure with an average ring current of 297 mA under ring operation at 2.5 GeV.

More than 40 Laue spots were recorded on the imaging plate. An important feature of the Laue pattern is that pairs of satellite reflections accompanied by missing main spots are observed (Fig. 9). This type of pyrrhotite series is classified as the NA type, and its *c*-axis is three-times longer than that of the niccolite (NiAs)-type subcell. The pairs of satellites indicate twinning of the NA type. From the positions of satellite reflections, the periodicity of the *a*-axis is estimated to be 41.84-times (N = 41.84) longer than that of the niccolite type FeS subcell. This mineral is entirely new regarding natural or synthetic materials.

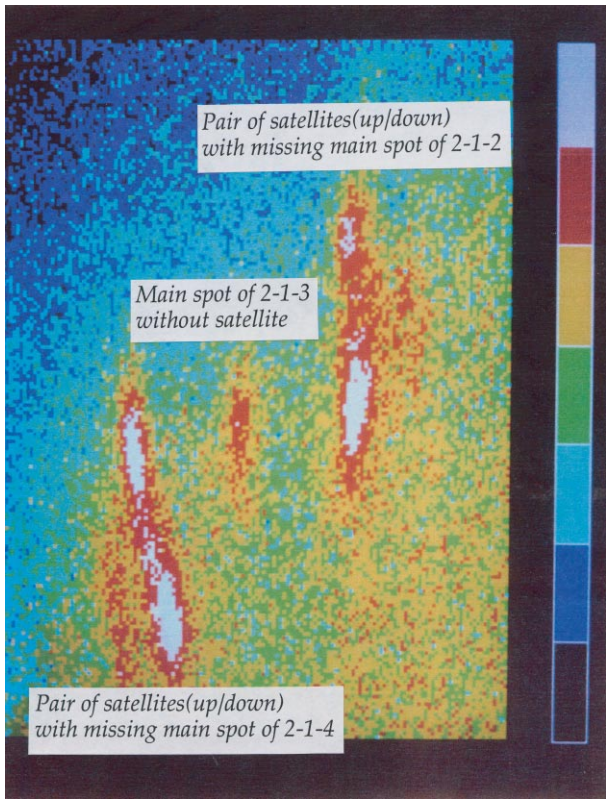

Figure 9
Pairs of satellite reflections accompanied by missing main spots indexed 2-1-2 and 2-1-4. The main spot with an index of 2-1-3 has no satellite reflections.

References

[1] Y. Murata, M. Murata, K. Komatsu, *J. Am. Chem. Soc.*, **125**(2003) 7152, *Chem. Eur. J.*, **9** (2003) 1600.
[2] H. Sawa, Y. Wakabayashi, Y. Murata, M. Murata and K. Komatsu, *Angewandte Chemie Int. Edit.*, **44** (2005) 1981.
[3] K. Meisel and Z. Anorg, *Allgem. Chem.*, **240** (1939) 300.
[4] I. Bransky, N. M. Tallan and A. Z. Hed, *J. Appl. Phys.*, **41** (1970) 1787.
[5] Y. Konoike, T. Toyoda, K. Yamawaki and S. Sasaki, *Proc. Sympo. Atomic-Scale Surf. Interf. Dynam.*, **4** (2000) 437.
[6] O. Berkooz, M. Malamud and S. Shtrikman, *Solid State Comm.*, **6** (1968) 185.
[7] F.L. Carter, *J. Solid State Chem.*, **5** (1972) 300.
[8] G. G ntherodt and W. Wichelhaus, *Solid State Commun.*, **39** (1981) 1147.
[9] H. Ohara, S. Sasaki, Y. Konoike, T. Toyoda, K. Yamawaki and M. Tanaka, *Physica B*, **350** (2004) 353.
[10] M. Yashima and M. Tanaka, *J. Appl. Crystallogr.*, **37** (2004) 786.
[11] M. Tanaka, M. Yashima and T. Mori, *in AIP Conference. Proceeding, 705 Synchrotron Radiation Instrumentation: Eighth International Conference on Synchrotron Radiation Instrumentation, edited by T. Warwick, J. Arthur, H. A. Padmore, J. Stöhr, Germany: Springer Press* (2004) 1055.
[12] F. Izumi and R. A. Dilanian, *in Recent Research Developments in Physics, Part II, Trivandrum, Transworld Research Network* **3** (2002) 699.

5-6-2 High Pressure Science

In PF high pressure experiments are carried out by two different kinds of pressure generating devices. One is the very compact pressure equipment named DAC (diamond-anvil cell), which can realize ultra-high pressure in the sample area of several dozen micro meter size. Special X-ray diffraction systems have been installed in Laser-Heating high-temperature and high pressure station BL-13A and the low and/or room-temperature high pressure station BL-18C. The other device is called the large volume press having a heavy frame and a strong hydraulic ram. There are two large volume press named MAX-III and MAX-80 installed in BL-14C2 and AR-NE5C, respectively. Both presses have been equipped the cubic-anvil high-pressure system which is the Japanese original device and used widely in the world.

New BL-13A Station constructed for in-situ Laser-heating High Pressure X-Ray Diffraction Experiments.

The X-ray diffraction system under high pressure and temperature originally installed at BL-13B2 was moved to the BL-13A which was newly reconstructed during the summer shutdown period of 2000 [13]. The new optics realized both higher resolution and intensity of the powder X-ray diffraction profile at the sample position. The large uncertainty of temperature measurements and chemical differentiation due to a long time exposure time [14] were drastically improved in BL-13A. Accordingly, several new users start their experiments in BL-13A.

Quasi-hydrostatic compression experiments using helium as a pressure-transmitting medium have been performed to utilize the high brilliance of BL-13A. Uniaxial stress is one of the serious problems in high-pressure experiments. In order to improve the sample environment under pressure, it is desirable to use soft and inert material as a pressure medium. Helium is the best material for the pressure medium that we know so far. However, the sample room under pressure becomes very small because of the highly compressible nature of helium. Therefore, ultra-high pressure data using helium is very limited and using a small beam as a probe is indispensable. In their experiments, the unit-cell volume of silicate, pressure maker (Au, MgO etc.) and pure elements under pressure up to about 200 GPa at maximum have been investigated with 20 - 30 μm collimator. These experiments will allow great progress in studies on the high-pressure behaviors of materials. For heating experiments, stability fields of high-pressure and high-temperature phase in some oxides and the reaction boundary of the iron-water system have been studied using a high-power multimode Nd:YAG laser.

A High Pressure and High Temperature in situ X-Ray Diffraction Study on FeO under Lower Mantle Conditions

The properties and behavior of FeO under lower mantle conditions play a key role in understanding the nature of the Earth's core and the core-mantle boundary. Shock compression studies [15,16] have clarified the existence of a phase transformation accompanied with a large volume change at around 70 GPa, while no such transition was found at room temperature compression up to 120 GPa [17]. A diamond-anvil experiment coupled with external heating clarified the existence of a B8-structured phase at an elevated temperature of around 1000 K [18], but many conflicting results [19] have been presented recently on the stability and the structure of the B8-type phase, and the nature of this phase transition is not yet clear.

High-pressure and high-temperature in situ X-ray diffraction studies have been carried out at BL-13A using a diamond-anvil cell coupled with YAG-laser heating [20]. A powdered FeO sample was sandwiched with Al_2O_3 powder as a thermal insulating layer and compressed to the desired pressure at room temperature. Then a thin X-ray beam of about 30 μm in diameter irradiated the sample and diffraction patterns were collected with increasing temperature. The sample was heated using a YAG-laser beam of about 60 μm in diameter through the diamond anvil. Example diffraction patterns are shown in Fig. 10. Just after the room temperature compression up to 80 GPa (bottom pattern) all the diffraction peaks are broad due to stress inhomogeneity within the sample, but the existence of rhombohedrally distorted FeO together with Al_2O_3 can be observed.

With increasing temperature, the FeO transforms into the B8 phase below 1000 K, and further transformation into the B1-structured phase can be seen at around 1500-1700 K. This B1-structured phase is unquench-

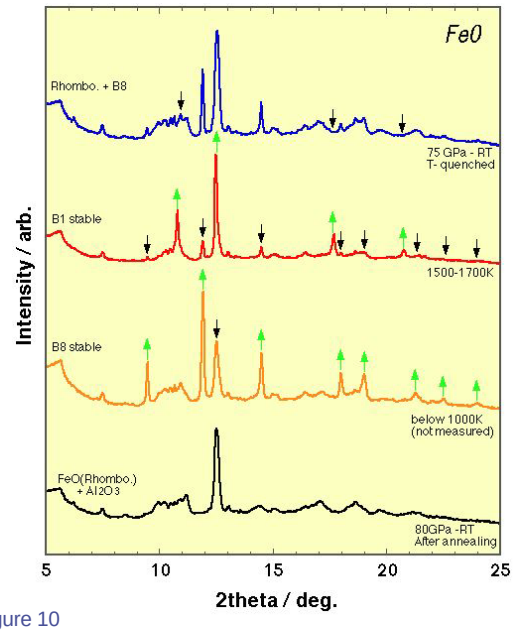

Figure 10
Examples of the high-pressure and high-temperature *in situ* X-ray diffraction patterns of FeO observed at around 80 GPa.

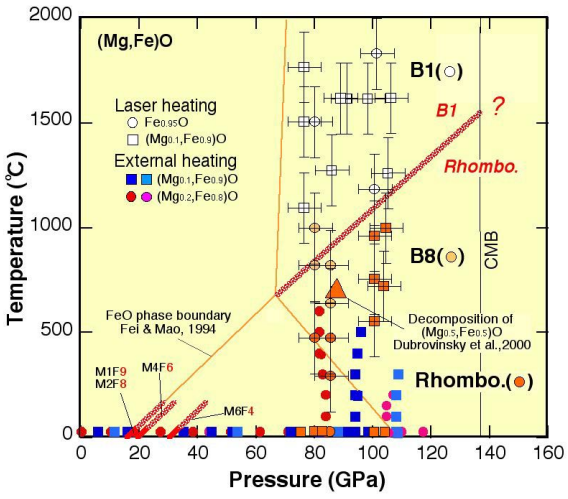

Figure 11
Phase diagram of FeO determined based on the present study. Three different phases exist under high-pressures and temperatures but the phase boundaries among these three phases have still ambiguity.

able upon lowering of the temperature, and only the rhombohedral and B8 phases of FeO were observed at room temperature after heating (top pattern). Such observations were repeated at various pressures up to about 120 GPa and the results are summarized in Fig. 11.

The present result [21] indicates that the stability fi eld of the B1 phase extends to very high pressures at high temperature while that of the B8 phase is limited to relatively low temperature. Considering the temperature distribution in the Earth's deep interior, it is likely that FeO remains unchanged with a B1-structured phase in the entire region of the Earth. However, this result is not in harmony with the results obtained by shock compressions [15,16]. A possible source of the discrepancy is the non-stoichiometric nature of FeO, and further studies on 1-xO with various stoichiometries are in progress.

The Modulated Structure of Solid Iodine during Molecular Dissociation under High Pressure

Solid iodine is a typical molecular crystal, in which four I2 molecules are arranged in an orthorhombic unit cell. The application of pressure to solid iodine forces the I2 molecules in the crystal to approach each other until intermolecular distances become comparable to the bond length of iodine; at this point, the molecules lose their identity and are essentially dissociated. This phenomenon, called pressure-induced molecular dissociation, was first observed in iodine at about 21 GPa in X-ray diffraction experiments [22]. Associated with the molecular dissociation, iodine undergoes successive structural phase transitions under high pressure; phase I (an orthorhombic molecular phase stable at ambient pressure), phase II (a body-centered orthorhombic phase stable above 21 GPa), phase III (a body-centered tetragonal phase stable above 43 GPa) and phase IV (a face-centered cubic phase stable above 55 GPa) [23]. Iodine molecules are dissociated in phases II, III, and IV.

Although X-ray diffraction experiments offer a simple picture of the molecular dissociation, some high-pressure experiments suggest more complicated behavior. Mössbauer [24] and Raman spectroscopy [25] experiments suggest that intermediate molecular phases may exist prior to the molecular dissociation.

In order to study the detailed structural change of iodine near the molecular dissociation, we have recorded powder X-ray diffraction patterns with high resolution by using a helium pressure-transmitting medium in a diamond-anvil cell and the intense synchrotron radiation from the multi-pole wiggler (MPW) of BL-13A and BM of BL-18C. The helium medium offers excellent quasi-hydrostatic conditions, thereby reducing pressure inhomogeneity in the sample chamber. It follows that one can specify a narrow pressure range without phase mixture. We found a new intermediate phase (phase V) in the pressure range 24-28 GPa. The crystal structure is incommensurately modulated, a rare case for the elements [26]. Figure 12 shows the crystal structures for phases I, V and II. The distances between the nearest-neighbor atoms of the intermediate phase are continuously distributed over the range from 2.86 to 3.11 Å (Fig. 13). The shortest of these interatomic distances falls be-

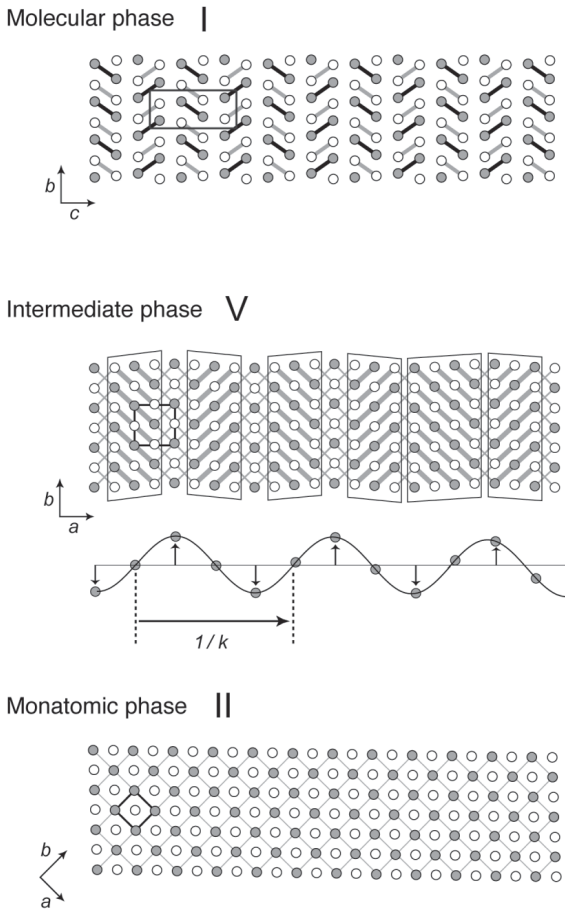

Figure 12
Crystal structure of iodine for phases I (19.1 GPa), V (24.6 GPa), and II (30.4 GPa).

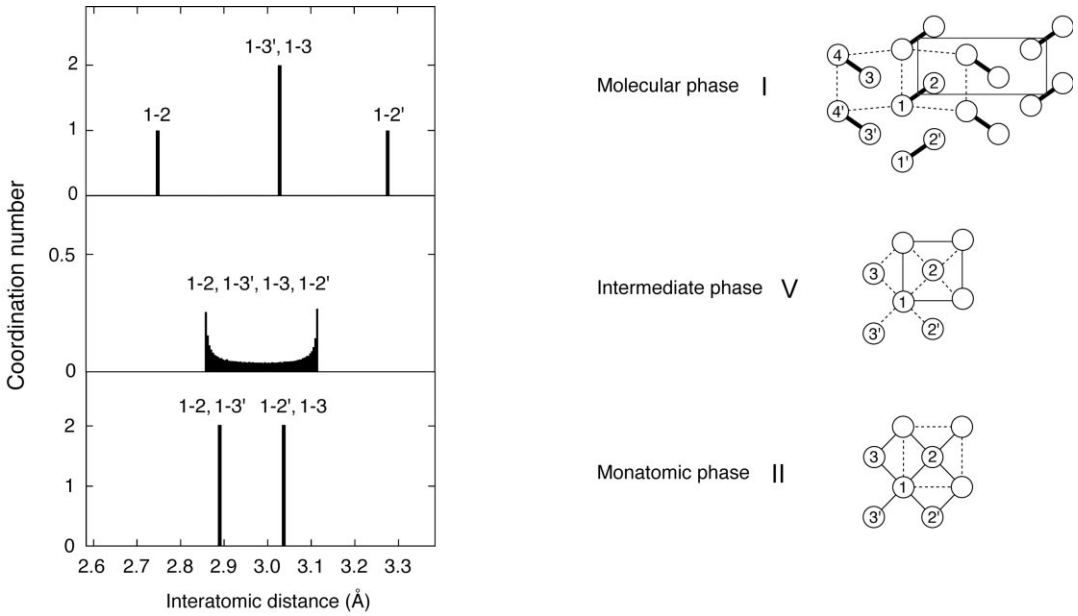

Figure 13
Distribution of the near interatomic distances for phases I (19.1 GPa), V (24.6 GPa), and II (30.4 GPa).

tween the bond length of iodine in the molecular crystal (2.75 Å) and the nearest interatomic distance in the fully dissociated monatomic crystal (2.89 Å). This means that the intermediate phase is a transient state during the molecular dissociation.

The origin of the existence of an incommensurate structure near the molecular dissociation is highly interesting. Further experiments at different temperatures are necessary to clarify the stability region of the incommensurate phase. The results may lead to a better understanding of the molecular-level mechanism of the molecular dissociation observed here, and those which can be expected for other molecular crystals like hydrogen, oxygen, and nitrogen.

Metastable garnet in the descending oceanic crust into the lower mantle.

As the oceanic plate descends into the Earth's lower mantle below the 660 km seismic discontinuity, garnet and silicate spinel, which are the major constituent minerals in the oceanic crust and the underlying peridotite layer, respectively, cause the decomposition reaction forming silicate perovskite (the post-garnet transformation and the post-spinel transformation, Fig.14). It has been suggested that these transformations are kinetically inhibited due to low temperatures in the plate and metastable low-pressure phases exist beyond the equilibrium boundary. Because the density increase ~10% caused by these transformations is much larger than the thermal density difference between the plate and the surrounding mantle, kinetics possibly affects the style of the mantle convection by determining whether cold plates (~700-1200°C) sink into the hot mantle (~1600°C). Therefore, in order to understand the dynamics of the descending cold plates into the lower mantle, it is indispensable to examine the kinetics of the post-garnet and the post-spinel transformations.

The kinetics of these transformations were observed at 26.7-31.0 GPa and 860-1850°C [27,28]. X-ray diffraction patterns of the sample were taken every 10-300 seconds by the energy dispersive method using SSD. We used a high-pressure in-situ X-ray diffraction system with a cubic-anvil high-pressure apparatus (MAX-80 and MAX-III) [29]. MAX-80 and MAX-III are 500-ton and 700-ton uniaxial presses, respectively, with cubic type guide-blocks. The latter has been newly installed (2000) in BL-14C2. Pressure was generated by the KAWAI type system consisting of six outer anvils loading an assembly of eight truncated cubic anvils. In order to generate more than 30 GPa, sintered diamond anvils were used as the second stage anvil [30]. Fig. 15 shows time dependence of the transformed volume fraction that was estimated from the decrease in the integrated intensity of diffraction lines in the parental phase. The post-garnet transformation was much slower than the post-spinel transformation.

Electron microscopy of the partially transformed sample revealed that these transformations are the grain-boundary reaction. Because the reaction rim of the decomposed assemblages was formed along the grain boundaries at the initial stage of the transformation, the overall transformation rate is controlled mainly by the growth kinetics. Based on the observed transformation mechanisms, the present kinetic data was analyzed using the rate equation $V = 1–\exp\{–2SX(t)\}$, where V is the transformed volume fraction, S is the area of the grain boundary, and $X(t)$ is the growth distance at time t [31]. The area of grain boundary can be expressed by 3.35/d, where d is the grain size of the parental phase. $X(t)$ is described by Kt^n ,where K and n are constants. The n-value was very small and less than 1 in the post-garnet transformation, which means that the growth rate

is time dependent and significantly decreases with time. This is different from the post-spinel transformation, in which the n-value was nearly 1 and the growth rate was almost constant. These differences in growth kinetics are believed to originate from differences in growth textures between these transformations [27, 28].

These are the first results of the direct measurement of the post-spinel and the post-garnet transformation kinetics by an in situ X-ray diffraction method. The rates of these decompositional transformations in the cold descending plate into the lower mantle were estimated by extrapolating the present kinetic data (Fig. 16). Our experimental results suggest that the post-spinel transformation can complete, however the post-garnet transformation is too slow to complete in geological time scales in the plates. Because a large amount of metastable garnet can survive in the descending oceanic crust into the lower mantle (Fig. 14), the oceanic crust would be buoyant in wider depth ranges at the top of the lower mantle taking the transformation kinetics into account.

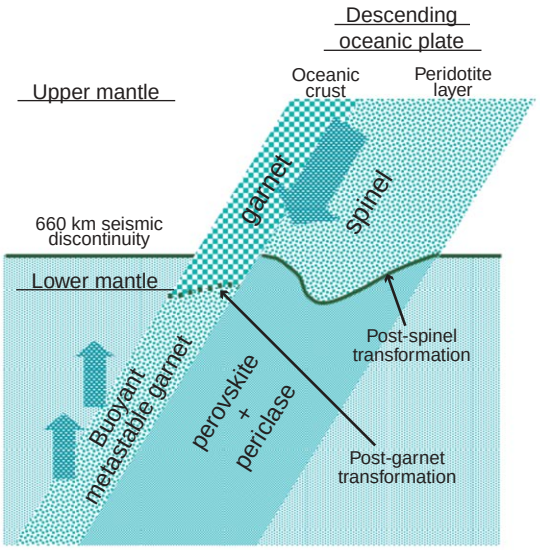

Figure 14
Schematic figure showing the cold descending oceanic plates grain boundary, and X(t) is the growth distance at time into the hot lower mantle. The post-spinel and the post-garnet transformations near the 660 km seismic discontinuity greatly affect dynamics of the descending plates and the style of the mantle convection

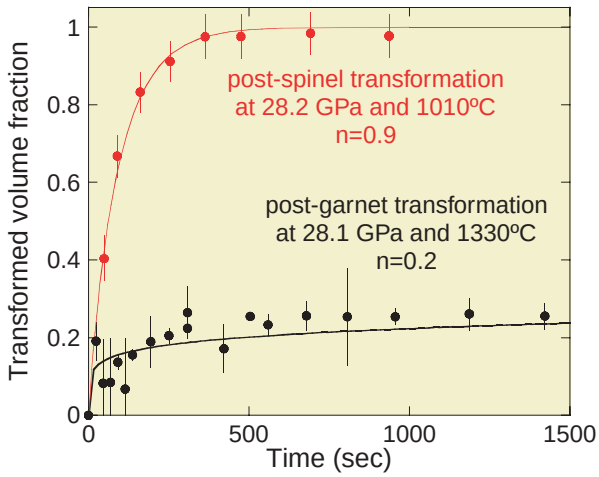

Figure 15
Transformed volume fraction with time in the post-spinel and post-garnet transformations. Curves obtained by the least-square fits of the rate equation to the kinetic data are also shown.

References

[13] See p. 72 of PF Activity Report 2000.
[14] T. Yagi et al., *Rev. Sci. Instrum*., **72** (2001) 1293.
[15] R. Jeanloz and T.J. Ahrens, *J. Roy. Astr. Soc.,* **62** (1980) 505.
[16] T. Yagi et al., Geohpys. *Res. Lett.,* **15** (1988) 816.
[17] T. Yagi, T. Suzuki and S. Akimotyo, *J. Geophys. Res.,* **90** (1985) 8747.
[18] Y. Fey and H. K. Mao, *Science*, **266** (1994)1678.
[19] e.g., R. Dubrovinsky et al, *Chem. Phys. Lett.,* **333** (2001) 264.
[20] T. Yagi et. al., *Rev. Sci. Instrum*., **72** (2001) 1293.
[21] T. Kondo et al., *Phys. Earth Planet. Inter*., in press.
[22] K. Takemura, S. Minomura, O. Shimomura and Y. Fujii, *Phys. Rev. Lett.*, **45** (1980) 1881.
[23] Y. Fujii, K. Hase, N. Hamaya, Y. Ohishi, A. Onodera, O.Shimomura and K. Takemura, *Phys. Rev. Lett.*, **58** (1987) 796.
[24] M. Pasternak, J. N. Farrell and R. D. Taylor, *Phys. Rev. Lett.*, **58** (1987) 575.
[25] H. Olijnyk, W. Li and A. Wokaun, *Phys. Rev. B*, **50** (1994) 712.
[26] K. Takemura, K. Sato, H. Fujihisa and M. Onoda, *Nature*, **423** (2003) 971.
[27] T. Kubo, E. Ohtani, T. Kato, S. Urakawa, A. Suzuki, Y. Kanbe, K. Funakoshi, W. Utsumi, T. Kikegawa and K. Fujino, *Phys. Earth Planet. Inter*., **129** (2002) 153.
[28] T. Kubo, E. Ohtani, T. Kondo, T. Kato, M. Toma, T. Hosoya, A. Sano, T. Kikegawa and T. Nagase, *Nature*, **420** (2002) 803.
[29] O. Shimomura, W. Utsumi, T. Taniguchi, T. Kikegawa and T. Nagashima, *Am. Geophys. Union, Geophys. Monogr. Ser.,* **67** (1992) 3.
[30] T. Kato, E. Ohtani, H. Morishima, D. Yamazaki, A. Suzuki, M. Suto and T. Kubo, *J. Geophys. Res*., **100** (1995) 20475.
[31] J.W. Cahn, *Acta Metall*., **4** (1956) 449.

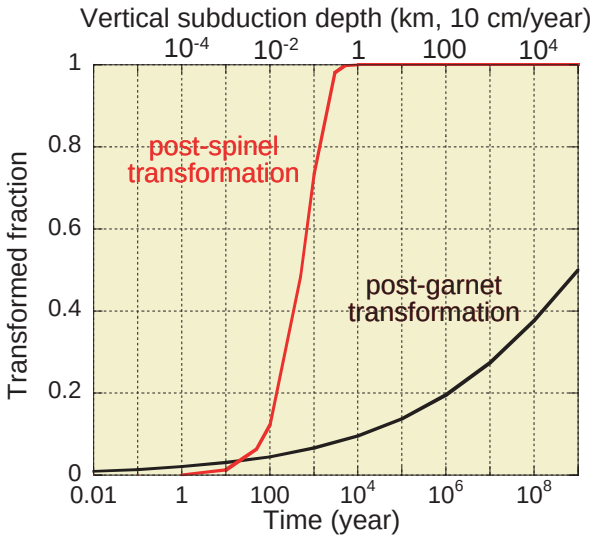

Figure 16
Rates of the post-spinel and post-garnet transformations in the descending plate into the lower mantle estimated by extrapolating the obtained kinetic data.